IVYSPRING INTERNATIONAL PUBLISHER

Nanotheranostics

2026; 10: 142-158. doi: 10.7150/ntno.132088

Research Paper

Small Extracellular Vesicles Reflect Senescence Progression in Human Bone Marrow–derived Mesenchymal Stem Cells During Hollow Fiber Bioreactor Culture

Ali Dinari[1]✉, Armin M. Ebrahimi[2,3], Bartosz Leszczynski[1], Kamil Wawrowicz[1], Masoud Rezaei[3,4], Maciej Słotwiński[1], Zenon Rajfur[2,5], Ewa L. Stepien[1,6]✉

1. Department of Medical Physics, M. Smoluchowski Institute of Physics, Faculty of Physics, Astronomy and Applied Computer Science, Jagiellonian University in Krakow, Poland.
2. Marian Smoluchowski Institute of Physics, Jagiellonian University in Krakow, 11 Łojasiewicza St., 30-348 Kraków, Poland.
3. Doctoral School of Exact and Natural Sciences, Jagiellonian University in Krakow, 11 Łojasiewicza St., 30-348 Kraków, Poland.
4. Faculty of Chemistry, Jagiellonian University, Gronostajowa 2, 30-387 Cracow, Poland.
5. Jagiellonian Center of Biomedical Imaging, Jagiellonian University, 30-348 Kraków, Poland.
6. Centre for Theranostics, Jagiellonian University, Kopernika 40 St, 31-501, Krakow, Poland.

✉ Corresponding authors: Ewa L. Stępień, Email: e.stepien@uj.edu.pl; Ali DinariEmail: alidinari606@gmail.com.

Received: 2026.01.25; Accepted: 2026.03.26; Published: 2026.05.26

Abstract

Prolonged three-dimensional culture exposes stem cells to sustain microenvironmental and mechanical stresses that can promote aging- and senescence-associated phenotypic alterations. This study examined how long-term expansion of human bone marrow–derived mesenchymal stem cells (BMSCs) in a hollow fiber bioreactor (HFB) influences cellular senescence and the molecular composition of secreted small extracellular vesicles (sEVs). During extended HFB culture, BMSCs exhibited progressive morphological flattening and cytoskeletal disorganization, accompanied by increased senescence-associated β-galactosidase activity and immunophenotypic remodeling characterized by reduced fluorescence intensity and spatial redistribution of canonical MSC markers, consistent with a stress-adapted, early senescence–associated cellular state. In parallel, sEVs were collected longitudinally over 40 days and characterized by nanoparticle tracking analysis, immunoblotting, and quantitative proteomics. While vesicle size, marker expression, and yield remained stable throughout culture, proteomic profiling revealed pronounced, phase-dependent remodeling of sEV cargo, including coordinated alterations in oxidative stress–related processes, lysosomal and extracellular matrix–associated pathways, and relative depletion of cytoskeletal and translational components. Notably, these vesicular signatures closely mirrored senescence-associated changes observed at the cellular level. The strong correspondence between cellular phenotypes and sEV proteomic profiles establishes vesicle analysis as a convergent and noninvasive readout of BMSC aging, enabling sensitive monitoring of senescence progression while reducing reliance on parallel, labor-intensive cellular assays. Collectively, these findings indicate that prolonged HFB culture promotes a controlled, stress-associated senescence program in BMSCs and position sEV proteomic profiling as a robust approach for assessing stem cell aging dynamics during long-term three-dimensional bioreactor culture.

Keywords: Small extracellular vesicles, mesenchymal stem cells, hollow fiber bioreactor, senescence, β-galactosidase, proteomics.

Introduction

Cellular aging and senescence are fundamental biological processes that regulate tissue homeostasis, regenerative capacity, and intercellular communication. In mesenchymal stem cells (MSCs),

senescence is characterized by progressive morphological enlargement, cytoskeletal remodeling, growth arrest, and altered expression of stemness-associated surface markers, ultimately impairing their functional potential and therapeutic utility [1,2]. These age-associated phenotypic changes are increasingly recognized as dynamic processes influenced by cellular microenvironment, metabolic stress, and prolonged culture conditions. Extracellular vesicles (EVs) have emerged as key mediators of cell–cell communication and reflect the physiological state of their parental cells. In particular, small extracellular vesicles (sEVs) carry proteins, lipids, and nucleic acids that mirror cellular stress responses, aging-associated signaling pathways, and senescence-related remodeling [3–6]. Accumulating evidence suggests that senescent or stress-adapted cells actively alter EV biogenesis and cargo composition, thereby propagating aging-related signals to surrounding cells and tissues [7]. For clinical and translational applications, large-scale and standardized production of MSC-derived EVs is required [8]. Conventional two-dimensional (2D) culture systems are limited in scalability and reproducibility, prompting the development of three-dimensional (3D) culture platforms that better support long-term cell expansion. Hollow fiber bioreactors (HFBs) provide a controlled 3D microenvironment with enhanced nutrient exchange and waste removal, enabling sustained, high-density MSC culture with reduced manual intervention [9–11]. HFB-based systems have been successfully applied for the production of recombinant proteins, viral vectors, and therapeutic nanovesicles, including MSC-derived EVs [12–15]. Despite these advantages, prolonged MSC culture, even under optimized conditions, can impose cumulative metabolic and mechanical stress that drives senescence-associated functional remodeling of both cells and their secreted vesicles [1]. While approaches such as genetic immortalization have been explored to overcome replicative senescence, MSCs inherently possess a finite lifespan, and culture-induced aging remains an unavoidable biological constraint [2]. However, how prolonged 3D culture shapes the senescence trajectory of MSCs and whether these changes are encoded within the molecular cargo of secreted sEVs remain incompletely understood. In this study, we investigated the effects of prolonged HFB cultivation on human bone marrow–derived MSCs (BMSCs), with a particular focus on senescence-associated cellular phenotypes and their relationship to longitudinal changes in sEV composition. BMSCs were expanded under conventional culture conditions and subsequently inoculated in HFBs for extended periods. Cellular aging was assessed using senescence-associated β-galactosidase staining, confocal microscopy, and flow cytometric immunophenotyping, while sEVs were characterized by nanoparticle tracking analysis, immunoblotting, and quantitative mass spectrometry. This integrated strategy enabled assessment of BMSC senescence at both cellular and vesicular levels, testing whether sEV molecular signatures provide a convergent readout of aging-associated cellular states under long-term 3D culture.

Materials and Methods

Materials

Bone marrow derived mesenchymal stem cells, (Cat#:PB-CH-675-0511-44-1), mesenchymal stem cell medium Kit enhanced xeno-free (Cat#:PB-C-MH-675-0511-XF) with 25 ml growth supplement, and cryo-gold, sterile filtered, endotoxin tested, 100 mL (Cat#, PB-10003-01) were purchased from PELOBiotech (Germany). FBS (Cat#: FBS-H1-11A) purchased from Capricorn Scientific company (GmbH, Germany). Cell culture medium such as DMEM high glucose (Cat#: 61965026), xeno-free medium (Cat: PB-C-BH-675-0511-XF) were purchased from PELOBiotech and Gibco companies respectively. Accutase enzyme solution (Cat#: 637945), PBS (Cat#:10010023), and three layers cell culture multi-Flask (#132867, DK-4000 Roskilde, Denmark) have been prepared accurately. Cartridge (Cat#: C2025D) purchased by Fiber Cell Systems (Maryland, USA). DAPI (4',6-diamidino-2-phenylindole) (Cat# 28718-90-3) and Phalloidin–tetramethylrhodamine isothiocyanate (Phalloidin-TRITC) (Cat#: R415) and Cellular senescence assay kit (Cat#: KAA002) were prepared from Poland.

Methods

Conventional two-dimensional (2D) cell culture

In brief, a batch of cryopreserved BM-MSCs was thawed (within 1.30 minutes at 37 °C in a water bath), mixed with 5 mL of fresh xeno-free medium, centrifuged (8 minutes at 500g), and cultured in a T75 flask. Three passages of cell culture were performed to obtain an adequate number of cells. Next, the cells were subculture into 7 three-layer multi-flasks cell culture. The seeding density was 1.5×10^6 cells per flask. At the proper confluency (90%) the cells were detached, centrifuged, resuspended in fresh xeno-free medium and transferred to intracapillary space (ECS) of HFBs.

Cell inoculation into HFBs

To inoculate the BMSCs into the HFBs, the harvested cells from conventional method were

centrifuged, resuspended in fresh medium and transferred to the ECS of HFBs. In this regard, the proliferated BMSCs were treated with accutase enzyme solution, centrifuged at 500g for 8 minutes and resuspended in the fresh complete DMEM (10% FBS). The total volume of resuspended cells solution was 3ml and was pipetted gently to prevent cell clumping. Next, the cells were transferred to a sterilized syringe, attached to the side port of the cartridge, and injected into the ECS of HFBs. To ensure complete filling of the cartridge space with cells, the suspension was gently pushed back and forth five times (Supplementary Methods, S1, S2).

HFB operation and maintenance

HFB performance was monitored to assess the physiological status of inoculated BMSCs throughout culture. Key parameters included glucose consumption, cell viability, and sEV recovery (Supplementary Methods, S3). Culture conditions including medium supply, temperature, and gas exchange were checked daily to ensure stable operation. BMSCs were initially cultured in high-glucose DMEM supplemented with 10% FBS. At mid-run, the culture medium was transitioned to a 1:1 mixture of DMEM and xeno-free medium (total volume 175 mL) and circulated continuously through the HFB lumen using a Duet pump system. During pre-culture and the first three days, the flow rate was maintained at 20–25 mL/min and subsequently increased to 30 mL/min for the remainder of the run. The hollow-fiber membrane (20 kDa molecular weight cut-off) permitted bidirectional exchange of nutrients and metabolic waste while retaining EVs within the ECS. sEV-containing medium was harvested from the ECS four times per week, collecting 3-3.2 mL per sampling. Medium recovered from the ECS was also used for assessment of BMSC viability. Distinct collection procedures were applied for sEV isolation and viability analysis.

Glucose consumption

To assess cell metabolic status, monitoring glucose consumption serves as an effective indicator. Indeed, glucose levels in the reservoir bottle reflect cell metabolic activity. In this case, the medium was collected from reservoir bottle and assayed by glucometer. The glucometer displayed values in units of mg/dL.

Cell viability

In addition to monitoring glucose consumption, which can be used as an indirect indicator of cellular metabolism, the viability of reside cells in the ECS of HFBs can be assessed by subculturing the detached cells. To this end, the BMSCs were harvested from HFBs and resuspended in the fresh medium and were seeded to T25 flasks. Through this experiment, the potency of detached BMSCs was evaluated.

EVs isolation

The sEVs were isolated from 4 mL of culture medium collected from the ECS using a differential centrifugation and ultracentrifugation protocol. Briefly, the conditioned medium was centrifuged at 500 × g for 10 min to remove cells and large debris, followed by sequential centrifugation at 3,000 × g for 25 min and 7,000 × g for 30 min to eliminate residual cellular contaminants. The resulting supernatant was further clarified by centrifugation at 18,000 × g for 20 min. Finally, small EVs were pelleted by ultracentrifugation at 150,000 × g for 90 min. The resulting sEV pellet was resuspended in PBS and stored at −80 °C until further analysis, in accordance with recommended extracellular vesicle handling procedures described in the MISEV2018 Guidelines. The sEV pellet was collected and used for downstream analyses (Supplementary Methods, S4).

Termination of HFBs operation

After a defined date, the HFBs operation system was terminated, and the cells were harvested and sub-cultured by conventional method. Through this stage, the effects of HFBs on cell morphology and viability were evaluated. The applied protocol for cell harvest is presented in Supplementary Methods (S5). In brief, the cartridge was treated with accutase enzyme, incubated at 37 °C for 1 hour and then flushed. Residual cells in cartridge's ECS were detached and flushing with PBS. This step should be handled by swishing the applied enzyme rigorously between two connected syringes to detect the cells. The solvent was transferred to the 15ml conical tube and centrifuged with condition of 10 minutes at 500g. Next, the cells were enumerated and checked for their viability. Afterward, the cells were cultivated in T25 flasks and incubated under optimum condition of incubator (37°C and 5% of Co_2) and didn't change the medium for three days. The process of cell proliferation and cell morphology were assessed correctly, and the results were recorded consequently.

BMSC characterization and senescence assessment

To evaluate the impact of HFB cultivation on BMSCs morphology three analytical techniques such as senescence-associated β-galactosidase (SA-β-Gal) assay, confocal microscopy, and flow cytometry were applied.

Cellular senescence assessment

Senescence was assessed using a commercially available SA-β-Gal staining kit following the manufacturer's protocol. BMSCs were seeded in six-well plates at two densities: 5 × 10^3 cells/well (≈20% confluency) and 2.5 × 10^4 cells/well (≈80% confluency). Cells were fixed with 1 mL of 1× fixing solution for 15 minutes at room temperature, washed twice with PBS, and incubated with 2 mL of freshly prepared 1× SA-β-Gal detection solution at 37 °C (without CO_2) for 4 hours. After incubation, the solution was removed, cells were rinsed with PBS, and blue-stained cells were quantified under a phase-contrast microscope. Increased blue coloration indicated enhanced β-galactosidase activity and senescence.

Confocal microscopy and cell staining

To visualize nuclear and cytoskeletal organization, DAPI and phalloidin staining were performed on fixed cells. DAPI stock solution (1 mg/mL) was diluted 1:1000 in PBS to a working concentration of 1μg/mL. Cells were incubated with DAPI for 10 minutes in the dark and rinsed twice with PBS. Permeabilization was achieved using 0.1% Triton X-100 for 10 minutes, followed by PBS washing and blocking with 3% BSA for 30–60 minutes at room temperature. Actin filaments were stained with Phalloidin–TRITC (100–200 nM) for 30–60 minutes in the dark. Cells were washed three times with PBS (5 minutes each) and imaged using a confocal laser scanning microscope. DAPI (excitation 358 nm; emission 461 nm) visualized nuclei, while Phalloidin–TRITC (excitation 540–555 nm; emission 570–580 nm) highlighted actin filaments.

Flow cytometry

Immunophenotypic characterization of BMSCs was performed using a CellStream™ flow cytometer (Model: CS 073; Manufactured: October 2020; USA). BMSCs were detached from T75 flasks, washed with cold PBS, and resuspended in PBS containing 2% FBS. Approximately 5 × 10^4 cells per sample were stained with 2 μL of each antibody in 100 μL PBS (2% FBS) for 30 minutes on ice in the dark. After two washes with PBS, the final cell pellets were resuspended in 200 μL PBS (2% FBS) for acquisition. The following antibodies were used for MSC characterization: CD105 (Cat# 2216090), CD90 (Cat# 2240590), CD73 (Cat# 2320020), and CD45 (Cat# 2120070) (Sony Biotechnology Inc.); and CD146 (Cat# 563619) and CD271 (Cat# 562122) (BD Biosciences).

Characterization of sEVs

To investigate the properties of BMSCs and their functional status during HFBs cultivation, sEVs were isolated and comprehensively characterized using nanoparticle tracking analysis (NTA), micro–BCA protein assay, western blotting, and high-resolution mass spectrometry (MS).

Nanoparticle tracking analysis (NTA)

The size distribution and concentration of sEVs were determined using a NanoSight NS500 system (Malvern Instruments, UK) equipped with a green laser and NTA software version 3.4 Build 3.4.4. The samples of sEV were diluted in sterile, filtered PBS to achieve optimal particle concentration. Analytical parameters were kept constant across all measurements (camera level 12, slider gain 245, detection threshold 2). The resulting data revealed overlapping size distributions typical of sEVs, with the predominant population exhibiting a hydrodynamic diameter consistent with exosomal vesicles.

Protein quantification by micro–BCA assay

The total protein content of sEV preparations was quantified using the micro–BCA protein assay kit (Thermo Fisher Scientific, USA). Briefly, 5 μL of each sEV sample was mixed with 145 μL PBS, followed by 150 μL of micro–BCA working reagent. The mixture was incubated at 37 °C for 2 h, and absorbance was measured at 562 nm using a microplate reader. Protein concentrations were calculated against a bovine serum albumin (BSA) standard curve.

Western blotting

Western blotting was performed to verify sEV identity and purity based on the presence of canonical vesicular markers. Antibodies against CD9 (Cat. #10626D), HSP70 (Cat. #sc-7298), and ARF6 (Cat. #sc-7971) were obtained from Santa Biotechnology (Japan). sEV lysates were prepared by mixing samples 1:1 with RIPA buffer and incubating on ice for 30 min with gentle agitation. Lysates were centrifuged at 13,500 rpm for 15 min at 4 °C, and the resulting supernatant was collected. Protein samples were mixed with 2× Laemmli buffer (1:1/4 v/v) containing 5% β-mercaptoethanol, heated at 100 °C for 7 min, and separated by SDS–PAGE (80 V stacking gel, 120 V resolving gel). Proteins were transferred onto PVDF membranes at 100 V for 1 h. Membranes were blocked in TBST containing 3% BSA for 1 h at room temperature, followed by overnight incubation at 4 °C with primary antibodies (1:1500 dilution in 1% BSA/TBST). After washing (3 × 5 min, TBST), membranes were incubated with rabbit anti-mouse HRP-conjugated secondary antibody (1:5000 dilution) for 1 h at room temperature. Chemiluminescent

detection was performed using HRP substrate (Cat. No. WBKLS0100, USA), and signal acquisition was carried out using a qTouch Western Blot Imager (China). Expression of CD9, HSP70, and ARF6 confirmed the vesicular nature and integrity of the sEVs.

Proteomic analysis of sEVs by mass spectrometry

High-resolution proteomic profiling of sEVs was performed using a Vanquish Neo UHPLC system (Thermo Fisher Scientific, USA) coupled to an Orbitrap Astral mass spectrometer operating in data-independent acquisition (DIA) mode. Peptides were separated on a C18 analytical column under optimized gradient conditions. Raw DIA data were processed using DIA-NN v2.1.0 for spectral library generation, peptide identification, and label-free quantification. The human UniProtKB reference proteome (20,663 sequences; downloaded September 19, 2025) was used as the search database, with a 1% false discovery rate (FDR) applied at both peptide and protein levels. Data normalization, principal component analysis (PCA), and statistical evaluation were performed in R Studio (v2024.12.1 Build 563), and downstream bioinformatic analyses (hierarchical clustering, GO enrichment) were conducted using Perseus v2.1.5.0. Only proteins consistently identified across biological replicates were included in the final dataset, ensuring robust proteomic characterization of sEVs derived from HFB-cultured BMSCs.

Proteomic data processing

Quantitative proteomic profiling was performed on small extracellular vesicles (sEVs) isolated from BMSCs at three culture phases (Phase 1, Phase 2, Phase 3), with three biological replicates per phase. Protein abundance values were obtained from the proteomic software and exported together with statistical outputs, including fold change, p-values, q-values, and test statistics. Pairwise differential expression analyses were conducted using the built-in Student's t-test framework of the proteomic platform.

Volcano plot generation

Volcano plots were generated for each pairwise comparison (Exo_2 vs Exo_1, Exo_3 vs Exo_1, Exo_3 vs Exo_2). Log_2 fold change (log_2FC) values were plotted on the x-axis and $-log_{10}(p)$ values on the y-axis using Microsoft Excel. Proteins were categorized as upregulated ($log_2FC > 1$, $p < 0.05$), downregulated ($log_2FC < -1$, $p < 0.05$), or non-significant ($p \geq 0.05$). Threshold lines marking $log_2FC = \pm 1$ and $-log_{10}(p) = 1.3$ were included to aid visualization. Differential expression categories were color-coded in all volcano plots.

Heatmap analysis

Heatmaps were produced to visualize expression patterns across the nine sEV samples using Morpheus (Broad Institute; https://software.broadinstitute.org/morpheus). Protein IDs and their normalized abundance values were extracted from the primary dataset, reorganized into a new Excel sheet, and subjected to row-wise z-score normalization. Log_2-transformed values were used for visualization. Hierarchical clustering of proteins and samples employed Euclidean distance and complete linkage. Color gradients represented relative abundance, enabling identification of coordinated phase-specific expression profiles.

Venn and UpSet intersection analyses

To examine shared and phase-specific differentially abundant proteins, proteins meeting the significance criteria ($|log_2FC| \geq 1$ and $p < 0.05$) were compiled for each comparison. Venn diagrams were generated using InteractiVenn website (10.1186/s12859-015-0611-3) to illustrate simple overlaps, while UpSet plots were constructed using Intervene (Khan A, Mathelier A. Intervene, 2017) to resolve higher-order

STRING analysis

Protein–protein interaction networks were analyzed using STRING v12 (https://string-db.org/). Lists of differentially abundant proteins were uploaded, and interaction evidence incorporated experimental data, curated databases, co-expression, and text mining. A high-confidence interaction threshold (score = 0.7) was applied. Networks were visualized with nodes representing proteins and edges representing interactivity. STRING functional enrichment was used to identify significantly overrepresented GO terms, KEGG pathways, and molecular processes within each upregulated and downregulated set.

Results and Discussion

MSC senescence is a progressive process characterized by morphological remodeling, metabolic reprogramming, altered surface marker expression, and irreversible proliferative arrest [16]. Accumulating evidence indicates that senescence markedly compromises MSC therapeutic efficacy and the bioactivity of their secreted factors, including EVs [17]. While genetic strategies such as immortalization have been explored to mitigate senescence, these approaches raise substantial biosafety and regulatory concerns and may alter fundamental MSC properties. HFBs represent a scalable and reproducible

three-dimensional (3D) culture platform capable of supporting high-density MSC expansion under controlled perfusion conditions [18]. By providing continuous nutrient exchange, a high surface-area-to-volume ratio, and reduced manual manipulation, HFBs improve process consistency compared with conventional two-dimensional (2D) culture [19]. Moreover, 3D culture systems more closely approximate key aspects of the *in vivo* MSC niche [20]. However, prolonged exposure to 3D mechanical constraints and sustained metabolic demand may impose cumulative stress, potentially accelerating senescence-associated phenotypic remodeling. This study investigated how extended HFB cultivation influences bone marrow–derived MSC (BMSC) physiology, senescence development, and extracellular vesicle output. We demonstrate that although HFBs support efficient initial cell expansion and metabolic stability, prolonged culture induces cytoskeletal reorganization, metabolic adaptation, and progressive loss of proliferative competence, consistent with a stress-associated senescent phenotype. These cellular changes are paralleled by pronounced remodeling of the secreted small EV (sEV) proteome, linking bioreactor-induced senescence to alterations in vesicle composition.

Cell inoculation, glucose consumption, and viability in the HFB

BMSCs were efficiently inoculated into the HFBs at high density (~6.5×10^7 cells), achieving uniform adhesion and rapid establishment of a confluent cell layer along the fiber surfaces. Early-phase culture was characterized by high cell viability and stable proliferation, indicating effective adaptation to the perfused 3D microenvironment. These findings confirm that the HFBs supports robust initial MSC colonization and growth under controlled conditions. To assess metabolic stability during prolonged culture, glucose consumption was continuously monitored as a surrogate marker of cellular activity and viability. MSCs are adapted to low-oxygen niches and rely predominantly on glycolytic metabolism; thus, sustained glucose utilization reflects preservation of metabolic homeostasis [21]. Throughout the 39-day culture period, glucose levels exhibited a steady-state consumption profile, indicating maintained metabolic activity despite increasing culture duration. Periodic medium exchange preserved nutrient balance, and a gradual transition to xeno-free conditions did not disrupt overall metabolic stability, underscoring the metabolic adaptability of MSCs within the HFB. Despite sustained glucose utilization, functional viability has progressively declined with extended culture duration (Figure 1, supplementary data, S_3). Cells harvested at early time points readily reattached and proliferated following transfer to 2D culture, whereas late-stage harvested cells showed reduced attachment efficiency, diminished proliferative capacity, and increased cell loss. This dissociation between maintained bulk metabolic activity and declining regenerative competence suggests that it is prolonged. HFB culture supports cellular survival but promotes cumulative mechanical and metabolic stress that compromises MSC functional integrity. Such stress-associated decline is consistent with early stages of senescence, in which metabolic activity persists despite loss of proliferative potential.

Post-HFB harvest reveals senescence-associated morphological and functional remodeling

To further evaluate the impact of extended HFB culture on BMSCs phenotype, residual cells were recovered from the ECS and replated under standard 2D conditions (Figure 1, F-H). Compared with the parental population, harvested cells exhibited marked morphological alterations, including loss of the characteristic elongated spindle shape, increased cell flattening, and irregular cell contours. These features are hallmarks of senescence-associated cytoskeletal remodeling and reduced mechanotransducive capacity. In parallel, harvested BMSCs displayed a pronounced reduction in proliferative activity and colony organization relative to control cells maintained exclusively in 2D culture. Decreased intercellular connectivity and disorganized growth patterns suggest impaired paracrine communication and altered secretory behavior following prolonged exposure to the HFB microenvironment. Given the central role of paracrine factors, particularly cytokines, growth factors, and EVs, in MSC-mediated tissue repair and immunomodulation, such changes are indicative of functional aging [22,23]. Consistent with this interpretation, senescent MSCs are known to exhibit reduced paracrine potency and diminished therapeutic efficacy [24–27]. Our observations indicate that prolonged HFB culture induces a phenotypic shift toward a senescence-associated state, characterized by preserved short-term survival but impaired regenerative and secretory function. These cellular alterations provide a mechanistic framework for understanding the progressive remodeling of sEV cargo observed during extended bioreactor operation.

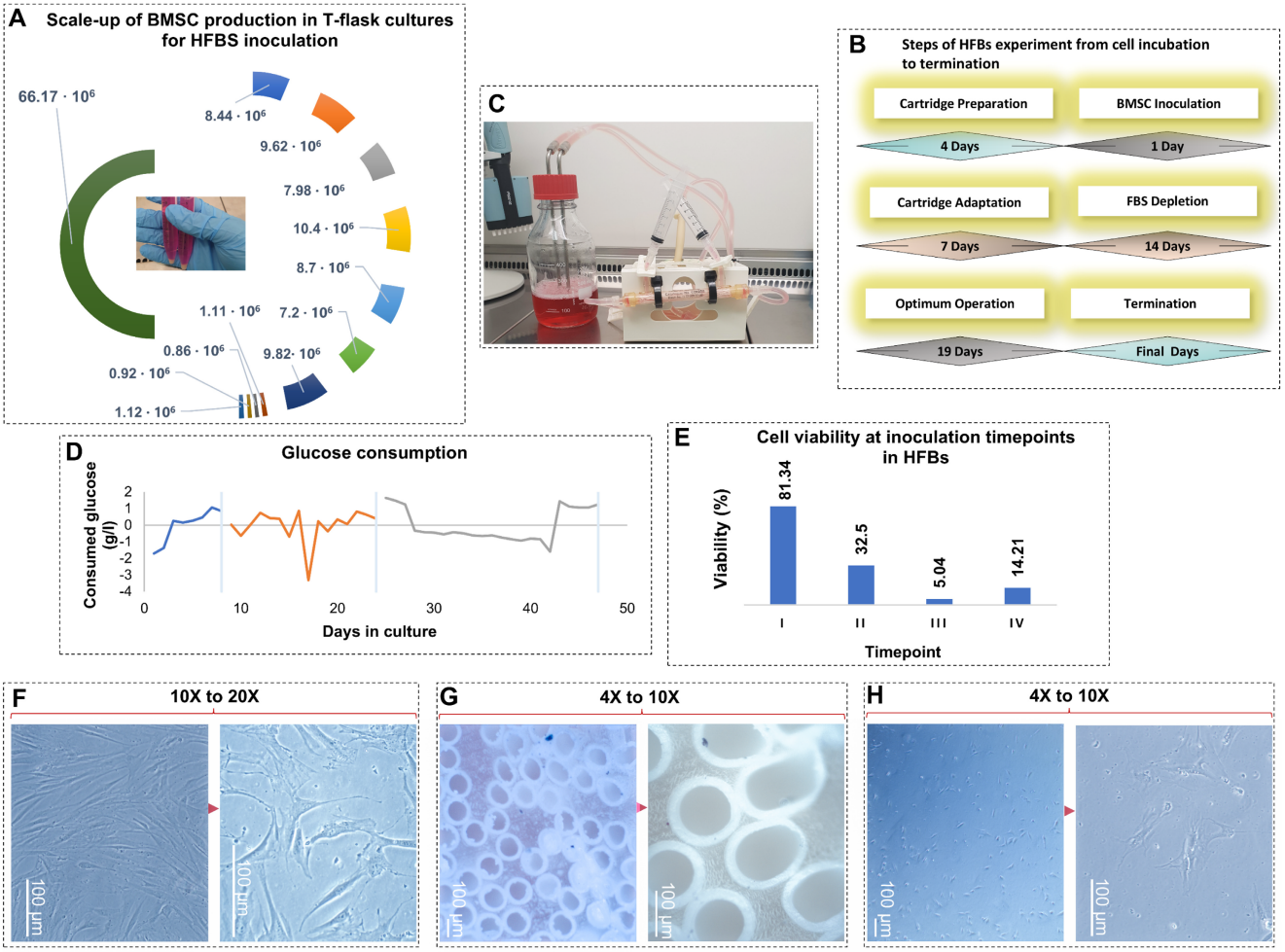

Figure 1. Scale-up, operation, and cellular responses of BMSCs during hollow fiber bioreactor (HFBS) culture. (A) Scale-up of human BMSC expansion in T-flasks prior to HFBS inoculation, illustrating cumulative cell yields obtained from different flask formats and passages used to achieve the required inoculation density. **(B)** Schematic overview of the HFBS experimental workflow, including cartridge preparation, cell inoculation, cartridge adaptation, stepwise fetal bovine serum (FBS) depletion, optimal operation phase, and system termination, with corresponding culture durations. **(C)** Representative image of the assembled HFBs setup during operation, showing the cartridge, tubing, and medium reservoir under continuous perfusion. **(D)** Glucose consumption profile over the course of HFBs culture, used as a surrogate marker of metabolic activity and viability. Shaded regions indicate distinct operational phases, including medium adaptation and extended culture. **(E)** Viability of BMSCs recovered from the ECS at defined inoculation/harvest time points, assessed after re-seeding under standard 2D conditions. **(F–H)** Representative phase-contrast microscopy images illustrating BMSC morphology under different culture conditions. (F) BMSCs maintained under conventional 2D culture display the characteristic elongated, spindle-shaped morphology (10×–20×). (G) BMSCs adhering to hollow fiber surfaces within the HFBs exhibit compact organization and altered spatial distribution (4×–10×). (H) BMSCs harvested from the HFBs and replated in 2D show flattened, irregular morphology and reduced cell density, consistent with senescence-associated remodeling (4×–10×). Scale bars are shown in each panel.

Characterization and senescence assessment of BMSCs cultured in HFBs

Senescence-associated β-galactosidase activity

To determine whether prolonged HFB culture induces cellular senescence, BMSCs harvested from the bioreactor were replated under standard conditions and assessed for senescence-associated β-galactosidase (SA-β-gal) activity (Figure 2-A). HFB-cultured BMSCs exhibited a marked increase in SA-β-gal activity, evidenced by intense cytoplasmic X-gal staining, whereas young, proliferative control BMSCs displayed negligible or absent β-galactosidase signal. SA-β-gal activity is a well-established hallmark of cellular senescence and reflects lysosomal expansion and altered metabolic homeostasis accompanying replicative and stress-induced aging. Consistent with prior studies, elevated SA-β-gal expression in BMSCs correlates with reduced proliferative capacity and progressive functional decline during cellular aging [28,29]. The heterogeneous staining pattern observed among HFB-derived BMSCs indicates the coexistence of senescent and non-senescent subpopulations, supporting the concept that senescence develops progressively and asynchronously within expanding BMSC cultures. These findings demonstrate that extended HFB cultivation promotes the emergence of a senescence-associated phenotype rather than uniform terminal arrest.

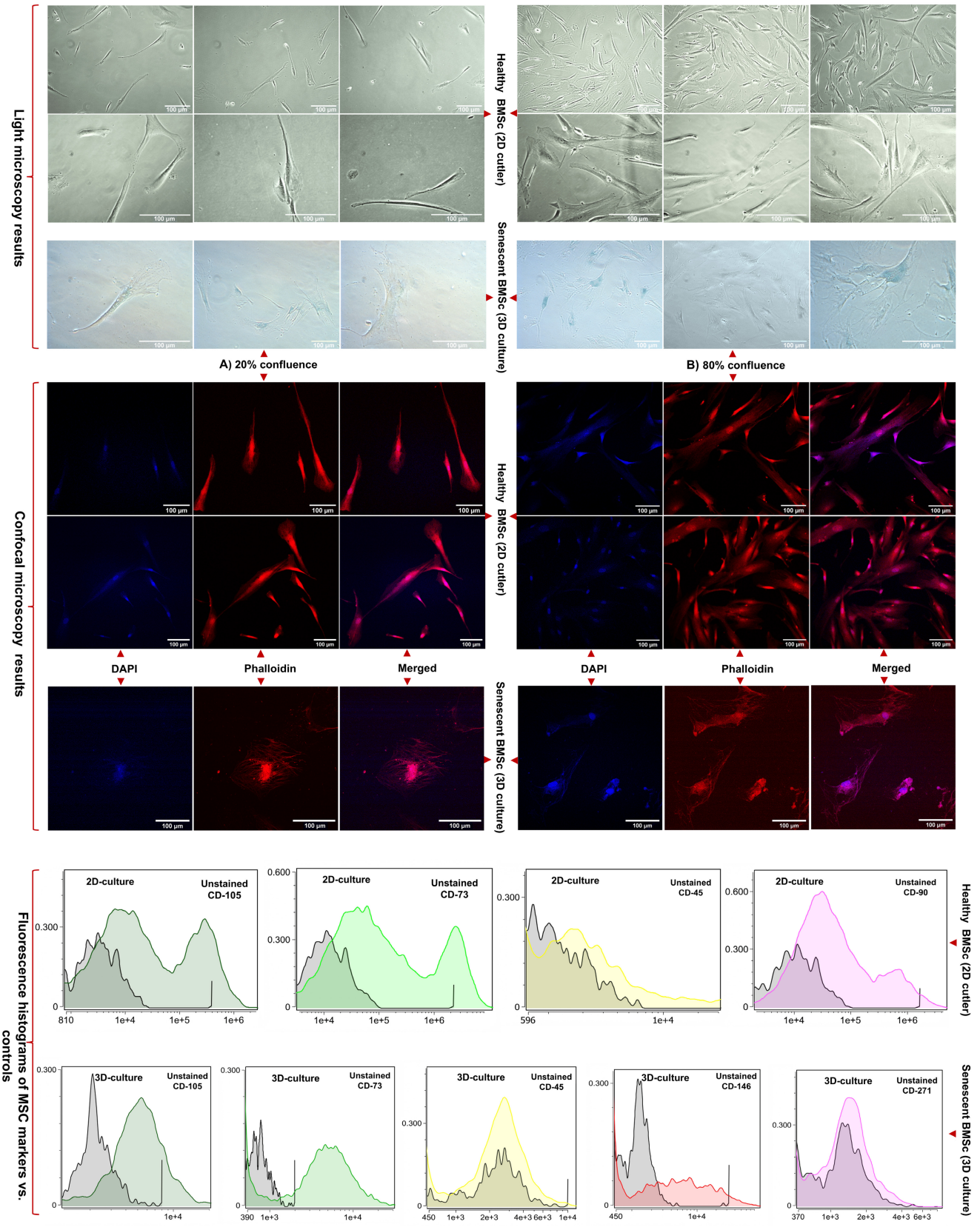

Figure 2. Representative light microscopy images show young BMSCs maintained under conventional 2D culture and senescent BMSCs harvested from 3D system at low (20%) and high (80%) confluence. Senescence-associated β-galactosidase (SA-β-gal) activity was markedly increased in HFB-cultured BMSCs, visualized by characteristic blue-green X-gal staining at pH 6.0, compared with minimal staining in young controls. Confocal microscopy following DAPI (nuclei) and phalloidin (F-actin) staining revealed pronounced cytoskeletal disorganization, cell flattening, and nuclear enlargement in senescent cells relative to spindle-shaped, highly organized young BMSCs. All microscopy images were acquired using a 20× objective. Flow cytometric analysis compares immunophenotypic profiles of BMSCs cultured under 2D and HFB conditions. Histogram overlays depict fluorescence intensity distributions of antibody-stained samples relative to unstained controls. HFB culture was associated with reduced fluorescence intensity and altered distribution profiles of classical MSC markers (CD105, CD73), while CD146 expression was maintained or modestly increased and CD271 expression showed greater variability.

Cytoskeletal and nuclear remodeling revealed by confocal microscopy

To further characterize structural alterations associated with senescence, BMSCs were examined by confocal microscopy following DAPI and phalloidin staining to visualize nuclear morphology and F-actin organization, respectively (Figure 2-B). Young BMSCs displayed the typical elongated, spindle-shaped morphology with well-organized, parallel actin filaments and uniformly shaped nuclei, reflecting preserved cytoskeletal tension and mechanotransductive signaling. In contrast, HFB-cultured BMSCs exhibited pronounced cytoskeletal remodeling, characterized by disrupted F-actin architecture, irregular filament accumulation, and loss of polarized organization. These cytoskeletal alterations were accompanied by nuclear enlargement, irregular nuclear contours, and reduced structural definition, indicative of compromised nuclear–cytoskeletal coupling and impaired cellular homeostasis. Such morphological features are characteristic of senescent MSCs and have been linked to altered mechanosensing, chromatin reorganization, and transcriptional dysregulation during cellular aging [30,31]. Taken together, the combined increase in SA-β-gal activity and the observed cytoskeletal and nuclear abnormalities provide convergent evidence that prolonged HFB culture induces a stress-associated senescence program in BMSCs. Importantly, these structural hallmarks of cellular aging parallel the functional decline and phenotypic remodeling described earlier, reinforcing the conclusion that HFB conditions, while supporting prolonged survival and metabolic activity, impose cumulative mechanical and metabolic stress that drives senescence rather than sustained stemness.

Flow cytometry was employed to assess immunophenotypic changes in BMSCs maintained under conventional 2D culture and following prolonged cultivation in HFBs. Surface markers associated with MSC identity, purity, and functional heterogeneity (CD105, CD90, CD73, CD45, CD146, and CD271) were analyzed to evaluate culture-induced phenotypic modulation (Figure 2-C, Supplementary Table, S1, S2), Supplementary Figures, S1)). Under standard 2D conditions, BMSCs exhibited robust expressions of CD105, CD90, and CD73, with negligible CD45 positivity, fulfilling the minimal criteria for MSC identity defined by the International Society for Cellular Therapy (ISCT) [32]. Fluorescence intensity histograms showed pronounced rightward shifts relative to unstained controls, with occasional bimodal distributions, consistent with intrinsic heterogeneity within proliferative MSC populations. The absence of CD45 expression confirmed the lack of hematopoietic contamination [33]. In contrast, BMSCs cultured in HFBs exhibited marked immunophenotypic remodeling. While CD105 and CD73 expression remained detectable, both the proportion of positive cells and, more prominently, fluorescence intensity distributions were reduced compared to 2D controls. Histogram compression and attenuation of high-intensity tails suggested a contraction of highly expressing subpopulation rather than complete loss of MSC-associated markers. These changes are consistent with phenotypic convergence under prolonged 3D culture conditions, potentially reflecting adaptive responses to sustained perfusion, altered nutrient gradients, and mechanical constraints within the HFB microenvironment. Expression of CD146 was maintained or modestly increased following HFB culture, in line with its association with perivascular-like MSC subsets and sensitivity to microenvironmental cues. In contrast, CD271 expression was more variable and generally reduced, suggesting selective modulation of more primitive or stem-like MSC subpopulations during extended culture. Together, these marker-specific shifts indicate a redistribution of functional MSC subsets rather than uniform phenotypic loss. Taken together, these data demonstrate that HFB cultivation induces immunophenotypic remodeling of BMSCs characterized by attenuation and redistribution of classical MSC markers and altered representation of stemness-associated subpopulations. While such changes are compatible with a stress-adapted or early senescence–associated state, definitive attribution to irreversible senescence requires complementary functional analyses. Importantly, the phenotypic state of EV-producing cells is known to influence extracellular vesicle biogenesis and cargo composition [34], providing critical cellular context for the subsequent analysis of BMSC-derived small extracellular vesicles.

Characterization of BMSC-derived sEVs produced in HFB culture

Approximately 70 mL of conditioned medium (3 mL per collection) was sequentially harvested from the ECS of the HFB system and subjected to comprehensive sEV characterization using nanoparticle tracking analysis (NTA), micro-BCA protein quantification, and western blotting. NTA measurements consistently revealed vesicle populations with a narrow size distribution predominantly below 200 nm, confirming enrichment of sEVs and excluding significant contamination by larger microvesicles or cellular debris. Quantitative comparison of particle concentration and total protein

content demonstrated a strong positive correlation between vesicle number and protein yield, indicating proportional cargo loading across samples (Figure 3, Supplementary Table, S3)). This relationship indicates that increases in sEV particle abundance are accompanied by corresponding increases in total vesicle-associated protein, reflecting coordinated regulation of vesicle release and bulk protein export. Importantly, this proportionality does not preclude substantial qualitative remodeling of sEV cargo, which is addressed in subsequent proteomic analyses. Notably, sEV output displayed a reproducible oscillatory pattern across the three defined operational phases of the HFB: (i) early cell adaptation (days 1–7), (ii) serum depletion (days 8–21), and (iii) transition to xeno-free conditions (days 22–40). Despite changes in medium composition and increasing culture duration, vesicle production remained sustained, with concentrations ranging from 3.9×10^8 to 8.2×10^9 particles/mL (mean ≈ 2.5×10^9 particles/mL). Such rhythmic fluctuations are consistent with emerging evidence that EV secretion and cargo loading are influenced by stress-responsive and temporally regulated cellular pathways [35,36]. In the context of prolonged HFB culture, these oscillations likely reflect adaptive secretory responses of BMSCs to cumulative metabolic, mechanical, and oxidative stress rather than simple growth-associated variation. Protein quantification by micro-BCA assay (Supplementary Figure, S2), revealed sEV protein concentrations ranging from 50 to 500 µg/mL, consistent with reported values for MSC-derived sEV preparations obtained under scalable culture conditions [37,38]. Importantly, maintained protein yields despite progressive cellular senescence suggest that secretory activity is preserved even as proliferative capacity declines, an observation aligned with the concept of a senescence-associated secretory phenotype (SASP), in which stressed or aging cells remain metabolically active while altering the qualitative nature of their secretome. Western blot analysis (Supplementary figures, S3) of representative sEV fractions confirmed the presence of established vesicular markers, including CD9, HSP70, and ARF6, detected at their expected molecular weights (~25, ~70, and ~20 kDa, respectively). The concurrent detection of tetraspanin (CD9), cytosolic chaperone (HSP70), and membrane-associated trafficking protein (ARF6) verifies vesicle integrity, endosomal origin, and preservation of canonical sEV identity. These protein signatures are consistent with previously characterized BMSC-derived sEVs and validate the purity of the isolated vesicle populations [34,39,40]. Taken together, these data demonstrate that the HFB system supports sustained and reproducible sEV production over extended culture periods, even as BMSCs undergo progressive senescence-associated phenotypic remodeling. Notably, the preservation of vesicle abundance and structural identity in the context of cellular aging indicates that HFB-expanded BMSCs retain secretory competence, while the qualitative evolution of sEV cargo addressed in subsequent proteomic analyses likely reflects adaptive, stress- and senescence-associated changes in the parental cell state. This integrated framework links prolonged bioreactor culture with MSC aging dynamics and phase-dependent remodeling of sEV content.

Proteomic analysis of sEVs by mass spectrometry

Quantitative mass spectrometry revealed a progressive reduction in the number of proteins detected in sEVs across the three defined HFB culture phases, declining from Phase 1 (5,071 proteins) to Phase 2 (4,415 proteins) and further to Phase 3 (3,337 proteins) (Figure 4A). Despite this contraction in proteome breadth, differential expression analysis (Student's *t*-test, $q < 0.05$) demonstrated extensive phase-dependent remodeling of sEV cargo. A total of 1,618 proteins were differentially regulated in Phase 3 versus Phase 1, compared with 579 in Phase 2 versus Phase 1 and 550 in Phase 3 versus Phase 2 (Figure 4B), indicating that the most pronounced proteomic divergence occurred between early and late culture stages. The overall reduction in detectable proteins by Phase 3 is therefore more consistent with cumulative culture-associated stress and the emergence of senescence-associated phenotypes in HFB-expanded BMSCs than with a decline in vesicle production itself. Cellular senescence is known to alter intracellular trafficking, translational capacity, and endolysosomal dynamics, resulting in selective restriction and reprogramming of EV cargo composition [8,41]. To further resolve the structure and functional implications of these proteomic changes, complementary analyses including volcano plots, hierarchical clustering heatmaps, overlap analyses (Ven diagram, UpSet plot), and functional enrichment using STRING were performed.

Volcano–Heatmap–STRING analysis reveals phase-dependent remodeling of BMSC-derived sEV cargo

Comparative proteomic profiling across HFB culture phases demonstrated marked, coordinated remodeling of sEV protein cargo (Figure 4C–G). Volcano plot analyses revealed numerous significantly regulated proteins in each pairwise comparison, with the greatest divergence observed

between Phase 1 and Phase 3 samples, consistent with progressive cellular adaptation to prolonged 3D culture. Hierarchical clustering of the union-regulated proteins resolved the data into two principal expression modules: one progressively enriched toward Phase 3 and another progressively depleted, indicating structured activation and suppression of distinct biological programs rather than stochastic proteomic drift [42,43]. The STRING network analysis (Supplementary Figures (S4) identified 71 upregulated and 148 downregulated functional clusters (≥5 proteins per cluster). Functional enrichment visualization showed that proteins enriched in late-phase sEVs were predominantly associated with extracellular matrix organization, adhesion signaling, vesicle biogenesis, and endolysosomal pathways, alongside immune and stress-responsive signaling modules, including RHO–ROCK, mTOR-associated signaling, and ER protein processing. Evidence of metabolic reprogramming was also apparent, with relative enrichment of lipid-handling and glycolytic pathways, whereas components of oxidative phosphorylation and several amino acid metabolic pathways were comparatively underrepresented. In contrast, proteins progressively depleted from sEVs over time were enriched for nuclear and biosynthetic processes, including RNA splicing, ribosome biogenesis, RNA polymerase II–mediated transcription, nucleosome organization, and core metabolic functions such as the TCA cycle and branched-chain amino acid degradation. The selective loss of these biosynthetic and transcriptional regulators is consistent with reduced proliferative capacity and translational output characteristic of aging and pre-senescent MSCs. These coordinated shifts indicate that late-phase sEVs are not globally enriched but instead selectively repackaged, favoring stress-adaptive, ECM-associated, immune-related, and vesicle-trafficking proteins, while progressively excluding proteins linked to growth, biosynthesis, and metabolic homeostasis. This pattern aligns with senescence-associated reprogramming of MSC secretory activity, including mTOR-linked metabolic remodeling, endolysosomal and exosome-biogenesis adaptation, altered mechanotransduction and adhesion signaling and the emergence of innate and inflammatory signaling components reminiscent of SASP-associated EV cargo [40,44–49]. Additional enrichment of pathways related to TGF-β signaling, DNA damage response, and stress-associated cell death further supports a transition toward a senescence-influenced secretory state that dynamically reshapes sEV composition during prolonged HFB culture [50,51].

Phase-dependent sEV proteome remodeling during prolonged HFB culture reflects progressive MSC aging

Venn and UpSet analyses were employed to quantify shared and phase-specific differentially expressed proteins across the three HFB culture phases (Figure 3). Both analyses revealed a strong predominance of phase-specific changes, with the largest unique intersection observed for downregulated proteins in Phase 3 versus Phase 1 (Exo-Down 3 vs 1; 560 proteins), followed by uniquely upregulated proteins in the same comparison (Exo-Up 3 vs 1; 402 proteins). In contrast, comparisons involving Phase 2 showed smaller unique sets, consistent with a gradual rather than abrupt remodeling of the sEV proteome during prolonged culture. Only a limited number of proteins were conserved across all phase comparisons: 21 proteins were consistently upregulated, and 6 proteins consistently downregulated across Exo-2 vs 1, Exo-3 vs 1, and Exo-3 vs 2. The small size of these shared intersections, relative to the extensive phase-specific sets, indicates that sEV cargo composition is highly sensitive to cumulative culture duration and microenvironmental transitions, rather than reflecting a static MSC secretory phenotype. This pattern is consistent with previous reports demonstrating that cellular stress and senescence drive selective, context-dependent remodeling of exosomal cargo rather than uniform shifts in protein abundance [52,53]. Mechanistically, the predominance of Phase 3–specific differentials indicate a progressive rewiring of endosomal sorting and cargo-selection pathways as BMSCs transition toward a stress-adapted, senescence-associated state. This selective cargo loading is increasingly recognized as a defining feature of senescent EV biogenesis, in which vesicles function as reporters of intracellular remodeling rather than passive byproducts of secretion [54]. Functional annotation of the 21 consistently upregulated proteins revealed enrichment for extracellular matrix (ECM) organization and structural remodeling components, including fibulins (FBLN1, FBLN4), tenascin (TNC), collagens (COL4A2, COL6A1, COL6A3), microfibril- and adhesion-associated proteins (AEBP1, SNED1, SVEP1), and matrix-modifying enzymes (OMD, CPXM2). This ECM-dominant signature indicates reinforcement of cell–matrix interactions and structural stabilization, processes closely associated with senescence-associated secretory phenotypes (SASP) and reduced regenerative plasticity. The presence of LMNB1 within sEVs further suggests nuclear-envelope stress and chromatin

reorganization, features characteristic of early-to-intermediate senescence states [48]. Concurrent enrichment of NUCB1 and DNAJC3 supports increased export of ER-stress and proteostasis-related signals via sEVs [55]. In contrast, the 6 consistently downregulated proteins were enriched for membrane-associated trafficking, transport, and signaling components, including CLDN11, LSAMP, RAI3/GPRC5A, FLOT1, and SLC38A1. Reduced abundance of FLOT1, a lipid-raft scaffolding protein implicated in non-clathrin endocytosis and exosome biogenesis [56], together with decreased SLC38A1, a glutamine transporter [57], suggests attenuation of vesicle trafficking efficiency and altered metabolic support. Downregulation of adhesion- and membrane-organizing proteins further indicates remodeling of sEV membrane composition as senescence progresses [58]. Notably, the opposing trajectories of ECM-associated proteins (e.g., fibulins, collagens) and membrane/trafficking regulators (e.g., flotillins) highlight a shift from an active, dynamic vesicle-sorting phenotype toward enhanced matrix stabilization and structural signaling. This transition aligns with established models of senescence-associated cytoskeletal reinforcement, extracellular matrix remodeling, and functional decline in long-term MSC cultures [59].

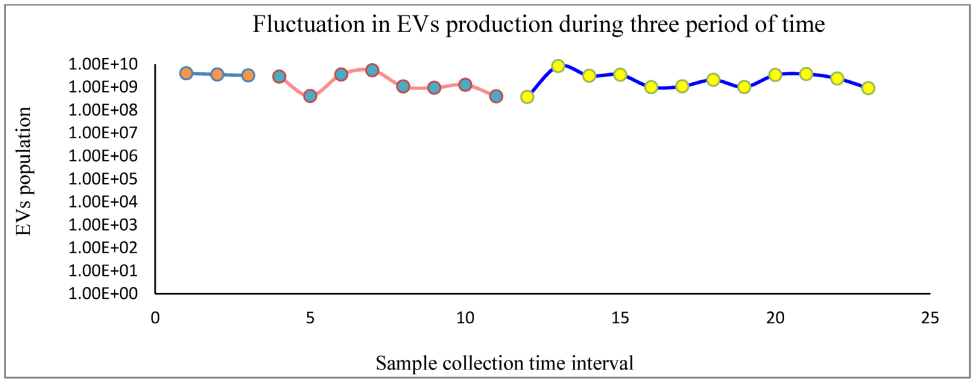

Figure 3. NTA analysis revealed that EV concentrations remained within the same order of magnitude (~10^8–10^9 particles/mL) across all three collection periods, indicating sustained EV production over time. While moderate fluctuations were observed within each phase, no abrupt drops or progressive declines were detected, suggesting stable bioreactor performance and cell viability. Notably, the later collection period showed slightly higher and more consistent EV yields, indicating adaptation and stabilization of EV secretion dynamics over prolonged culture.

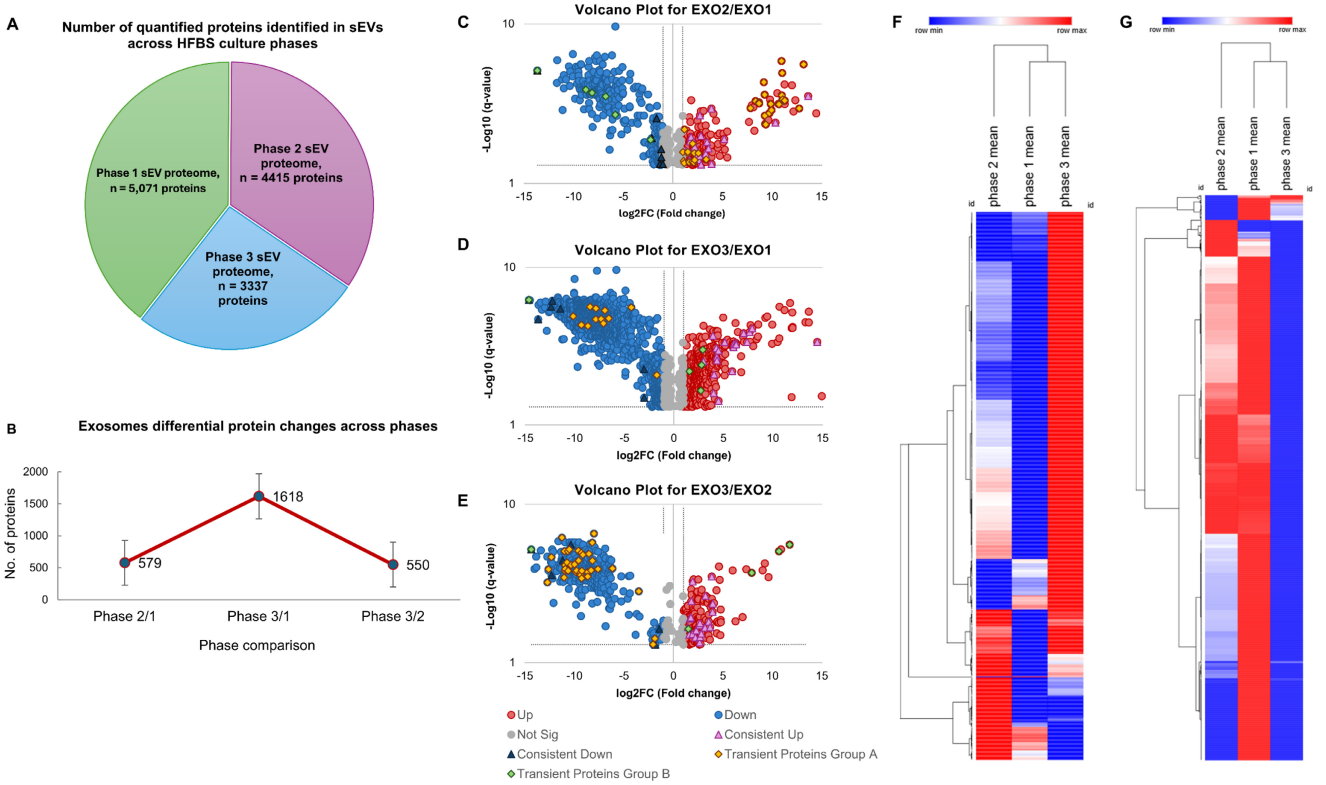

Figure 4. (A) the number of quantified proteins in sEVs across the three phases of HFBs culture. **(B)** Differential exosome protein expression across experimental phases. Line plot showing the number of exosomal proteins with significant differential abundance between sequential culture phases (Phase 2/1, Phase 3/1, and Phase 3/2). Error bars

represent variability across replicates. The largest proteomic shift occurred between Phase 3/1 (1618 proteins), followed by Phase 2/1 (579 proteins) and Phase 3/2 (550 proteins), indicating dynamic remodeling of the exosome proteome across the culture timeline. **(C, D, E)** Volcano plots showing phase-wise differential protein abundance (C: Exo2 vs. Exo1; D: Exo3 vs. Exo1; E: Exo3 vs. Exo2). Red and blue points indicate significantly upregulated and downregulated proteins, respectively; grey points denote non-significant changes ($|\log_2 FC|$ and adjusted p-value thresholds applied). It is noteworthy that the pink and black triangular symbols indicate proteins that are consistently upregulated or downregulated across all three phases. In contrast, the orange and green diamond-shaped symbols represent transient proteins, which are described in detail in the following sections. The complete lists of consistently regulated and transient proteins are provided in Supplementary Table S4. **(F–G)** Heatmaps of significantly regulated proteins across phases. Panel (F) highlights proteins progressively upregulated toward later phases, whereas (G) shows proteins with inverse or phase-specific downregulation. Rows represent proteins; columns show mean phase expression; colors reflect row-wise z-scores (red: higher; blue: lower).

Transient phase-dependent s EV' proteins define multistage senescence adaptation

Venn-intersection analysis revealed discrete subsets of transiently regulated sEV proteins exhibiting directionally opposing expression across culture phases rather than monotonic change, indicating stage-specific remodeling of exosomal cargo during prolonged HFB culture. Heatmap analysis of them confirmed pronounced direction-switching behavior, with proteins transiently induced during intermediate phases and subsequently suppressed at later stages, consistent with adaptive but ultimately constrained cellular responses during senescence progression [52,53]. One dominant protein module comprised factors linked to cell division, RNA metabolism, and adhesion-dependent mechanotransduction, including HMGB1, NOP56, TCOF1, U5-20k (U520), SRSF1, RBM25, GALT, STX16, CERT, LRRC15, RBP1, BKRB1, CLDN11, LSAMP, RAI3, SLC38A1, and FLOT1. Proteins involved in ribosome biogenesis and RNA splicing (NOP56, TCOF1, SRSF1, RBM25, U520) are essential for proliferative capacity and are known to decline during senescence-associated cell-cycle arrest and reduced biosynthetic output [44,60]. Concurrent downregulation of adhesion- and membrane-associated proteins governing lipid-raft organization, junctional stability, and mechanotransductive signaling (e.g., FLOT1, CLDN11, LSAMP, STX16, CERT) indicates early disruption of cytoskeletal tension sensing and cell–matrix communication, hallmark features of pre-senescent mechanobiological stress responses [45,61]. A second transient module displayed oscillatory regulation, characterized by suppression in Phase 1, induction in Phase 2, and renewed downregulation in Phase 3. This group included proteins involved in metabolic homeostasis, redox buffering, membrane trafficking, and paracrine signaling, such as MAT2A (METK1), ALDH1L1, PGAM4, KYNU, GSTA1/2, XDH, ALDH8A1, DPYS, SEC20, PLA1A, AREG, NOG, PTHR1, VEGFR3 (FLT4), and ANGPT1. These pathways regulate glycolytic flux, one-carbon metabolism, antioxidant defense, vesicular transport, and growth factor signaling, all of which are dynamically modulated during early senescence as cells attempt to buffer mitochondrial and cytosolic stress [62]. Their transient induction during the intermediate phase suggests an adaptive stress-mitigation program that becomes progressively disengaged as cells transition toward a stabilized senescence-associated state. A smaller subset exhibited delayed re-expression at late culture stages, including RTN1, SHH, ANGPT1, and CA13, implicating compensatory ER–Golgi remodeling, morphogen signaling, vascular/paracrine regulation, and pH-linked metabolic adjustment during advanced senescence [48,51]. Collectively, these data demonstrate that BMSC senescence under prolonged HFB culture proceeds through multistage, adaptive remodeling of exosomal pathways rather than a linear degenerative process. Early loss of proliferative and adhesion programs is followed by transient metabolic and paracrine compensation, culminating in stabilization of a senescence-associated secretory phenotype. The presence of reversible and phase-specific sEV signatures underscores the plasticity of MSC aging trajectories and establishes sEV proteomics as a sensitive, integrative readout of senescence stage, mechanotransductive stress adaptation, and functional decline in bioreactor-expanded BMSCs [47,54]. Senescence progression under prolonged HFB culture is therefore more accurately described as a continuous, quantitatively regulated biological process rather than a discrete phenotypic transition. Whereas conventional cellular assays primarily capture integrated or downstream manifestations of stress adaptation, longitudinal sEV proteomic profiling resolves coordinated, multiaxial remodeling across metabolic, cytoskeletal, redox, and extracellular matrix–associated protein networks. The concerted regulation of functionally interconnected protein modules indicates that senescence reflects a system-level cellular reprogramming event. In this context, sEVs act as integrative molecular reporters of intracellular aging dynamics, providing higher-resolution insight into senescence trajectories than endpoint cellular measurements alone. While the present study focused on the physicochemical and proteomic characterization of sEVs, future investigations should also examine the RNA and small RNA cargo of EVs, as transcriptomic profiling may provide additional insight into senescence-associated molecular signaling and EV-mediated intercellular communication [63–65].

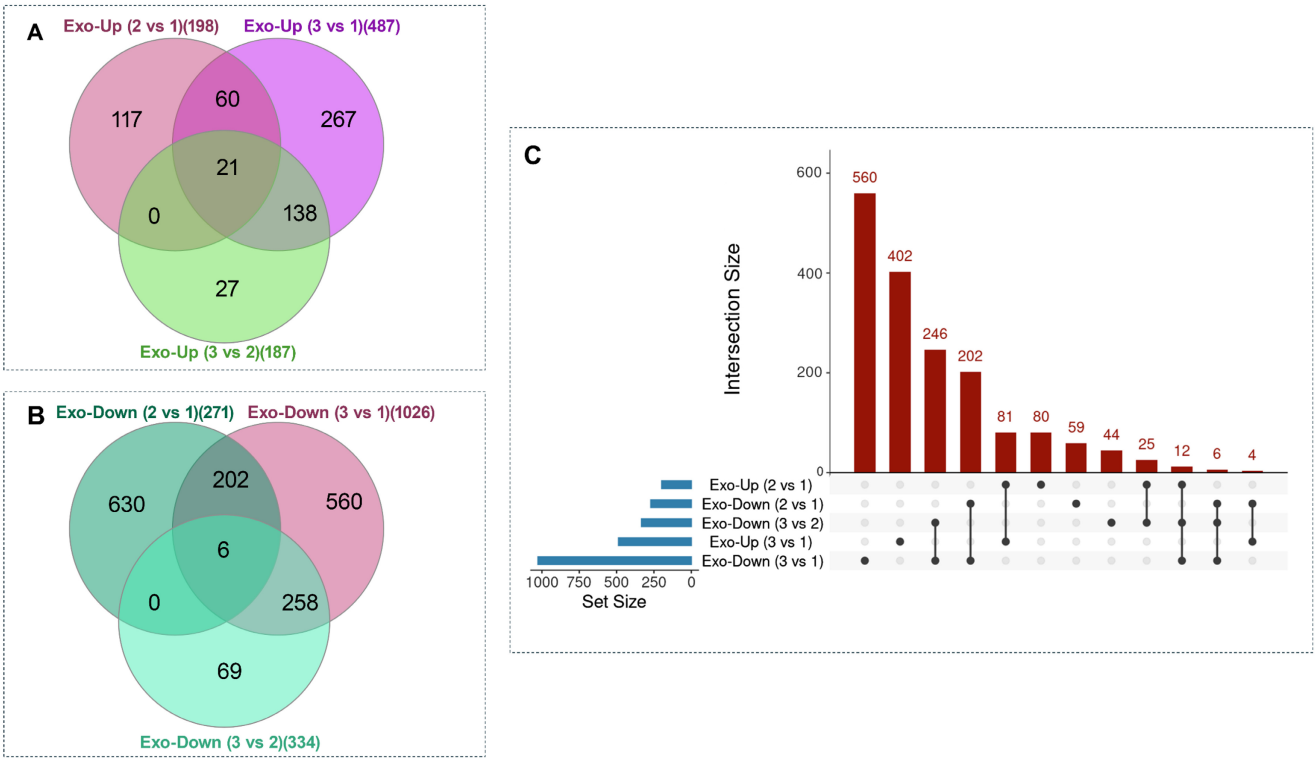

Figure 5. Venn and UpSet analyses of differentially expressed exosomal proteins across culture phases. (A–B) Venn diagrams illustrate the overlap among pairwise phase comparisons for upregulated (A) and downregulated (B) exosomal proteins across three phases of HFB operation. Across all three comparisons, a cluster of 21 proteins was consistently upregulated, while a cluster of 6 proteins was consistently downregulated. **(C)** UpSet plot summarizing set sizes and intersection patterns of all differentially expressed proteins. To avoid the visual complexity inherent to multiple Venn diagrams and to enable integrated visualization of both up- and downregulated proteins within a single framework, an UpSet representation was employed. In the UpSet plot, each column represents a unique intersection of protein sets; black dots indicate the participating comparisons, and vertical connecting lines denote simultaneous inclusion across those sets. The height of the bars above each column corresponds to the number of proteins within the respective intersection. This analysis highlights both consistently regulated proteins across all phases and transient, phase-specific regulatory patterns. When all up- and downregulated proteins were considered together, the largest unique intersections corresponded to Exo-Down (3 vs 1) (560 proteins), followed by Exo-Up (3 vs 1) (402 proteins), with additional major intersections indicated by bar labels. Collectively, these distributions reveal extensive phase-dependent remodeling alongside shared alterations in exosomal cargo composition.

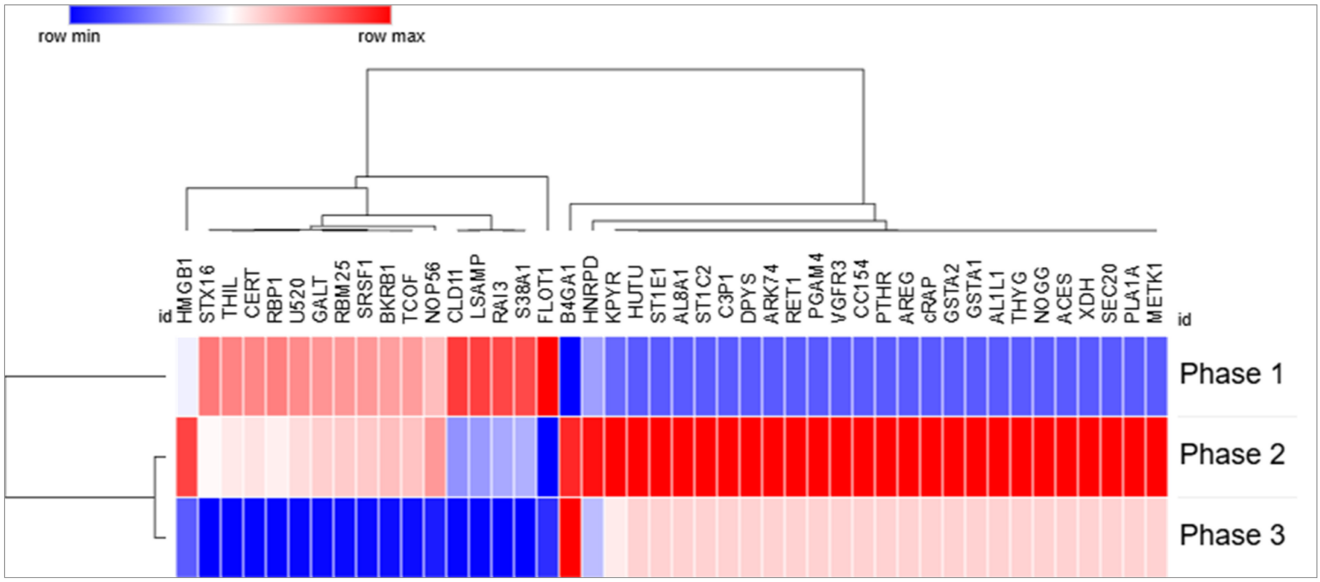

Figure 6. Transient phase-dependent remodeling of sEV protein cargo during prolonged HFB culture. Heatmap representation of exosomal proteins identified from Venn-intersection analyses showing non-monotonic, direction-switching regulation across culture phases. Rows correspond to individual proteins and columns to Phase 1, Phase 2, and Phase 3; protein abundance values are row-wise z-score normalized. Hierarchical clustering highlights distinct temporal expression patterns, including proteins that progressively decline from Phase 1 to Phase 3, predominantly associated with cell-cycle regulation, RNA processing, and cell–adhesion dynamics (e.g., HMGB1, SRSF1, RBM25, NOP56, STX16), as well as a second group displaying transient induction in Phase 2 followed by suppression in Phase 3, consistent with short-lived adaptive metabolic, stress-response, and paracrine signaling programs during senescence progression.

Conclusions and Future Perspective

Prolonged culture within a HFB supports sustained expansion of human BMSCs while progressively reshaping their physiological state through cumulative microenvironmental and mechanical stress. Integrated cellular analyses including morphological assessment, senescence-associated β-galactosidase staining, confocal imaging, and flow cytometry revealed the emergence of an adaptive, early senescence–associated phenotype marked by cytoskeletal reorganization and reduced proliferative competence. Importantly, preservation of core mesenchymal surface marker expression indicated that lineage identity was largely maintained despite stress-induced aging. The sEVs closely mirrored these cellular transitions. NTA, protein quantification, and immunoblotting confirmed stable vesicle size distribution, marker expression, and production efficiency throughout extended culture, indicating preserved vesicle biogenesis. In contrast, quantitative proteomic profiling uncovered pronounced, stage-dependent remodeling of sEV cargo. Early culture phases were characterized by enrichment of proteins associated with metabolic and redox homeostasis, followed by increased representation of stress-response and cytoskeletal regulators, and culminating in the accumulation of extracellular matrix–associated and senescence-linked signaling components. This temporal progression delineates a continuum from cellular stress adaptation to stabilization of a senescence-associated secretory phenotype. Collectively, these findings indicate that long-term HFB culture promotes a controlled, stress-associated aging trajectory in BMSCs rather than acute functional deterioration. The close correspondence between cellular senescence phenotypes and sEV proteomic signatures establishes vesicle profiling as a sensitive, noninvasive, and integrative readout of stem cell aging in bioreactor systems. From a translational perspective, this convergence suggests that sEV analysis can capture key aspects of cellular aging while reducing reliance on parallel, labor-intensive cellular assays. More broadly, this work provides a mechanistic framework linking bioreactor-imposed stress, adaptive senescence, and dynamic extracellular vesicle remodeling, informing the rational design and monitoring of scalable stem cell culture platforms for regenerative and therapeutic applications.

Supplementary Material

Supplementary methods, figures and tables.
https://www.ntno.org/v10p0142s1.pdf

Acknowledgements

We acknowledge Proteomics Core Facility of the Faculty of Biochemistry, Biophysics and Biotechnology and the Malopolska Centre of Biotechnology at the Jagiellonian University for mass spectrometry analysis. The purchase of Orbitrap Astral Mass Spectrometer has been supported by a grant from the Priority Research Area (POB BioS) under the Strategic Programme Excellence Initiative at Jagiellonian University.

Funding

This work was financially supported by funding from Narodowe Centrum Nauki (NCN) agency with a grant number of Reg. No: 2022/45/B/NZ7/01430.

Data availability

The row data are deposited in the RODBUK public repository (https://doi.org/10.57903/UJ/GIM176).

Author contributions

Ali Dinari: Conceptualization, methodology, data analysis, visualization, writing original draft, review and editing. Armin M. Ebrahimi: Microscopy imaging and related data analysis. Bartosz Leszczyński: Data visualization and graphical analysis. Kamil Wawrowicz: HFBs methodology. Masoud Rezaei: Methodology and imaging analysis. Maciej Stotwiński: NTA methodology. Zenon Rajfur: Microscopy imaging assessment. Ewa L. Stępień: Conceptualization, methodology, supervision, funding acquisition, review and editing.

Competing Interests

The authors have declared that no competing interests exist.

References

1. Boulestreau J, Maumus M, Rozier P, Jorgensen C, Noël D. Mesenchymal Stem Cell Derived Extracellular Vesicles in Aging. Front Cell Dev Biol. 2020; 8: 107.
2. Hayflick L. The limited in vitro lifetime of human diploid cell strains. Experimental Cell Research. 1965; 37: 614–36.
3. Kasprzyk-Pochopień J, Kamińska A, Mielczarek P, Porada R, Stępień E, Piekoszewski W. The Proteomic Analysis of Platelet Extracellular Vesicles in Diabetic Patients by nanoLC-MALDI-MS/MS and nanoLC-TIMS-MS/MS. Molecules. 2025; 30: 1384.
4. Skalska ME. Lipid analysis in biological structures – Is time-of-flight secondary ion mass spectrometry a valuable tool in nano-lipidomics? Bio-Algorithms and Med-Systems. 2025; 21: 8–19.
5. Skalska M, Durak-Kozica M. Experimental and analytical procedures for the ToF-SIMS measurement data of membranous structures. Bio-Algorithms and Med-Systems. 2023; 19: 64–8.
6. Théry C, Witwer KW, Aikawa E, et al. Minimal information for studies of extracellular vesicles 2018 (MISEV2018): a position statement of the International Society for Extracellular Vesicles and update of the MISEV2014 guidelines. J of Extracellular Vesicle. 2018; 7: 1535750.
7. Welsh JA, Goberdhan DCI, O'Driscoll L, et al. Minimal information for studies of extracellular vesicles (MISEV2023): From basic to advanced approaches. J of Extracellular Vesicle. 2024; 13: e12404.

8. Gobin J, Muradia G, Mehic J, et al. Hollow-fiber bioreactor production of extracellular vesicles from human bone marrow mesenchymal stromal cells yields nanovesicles that mirrors the immuno-modulatory antigenic signature of the producer cell. Stem Cell Res Ther. 2021; 12: 127.
9. Greuel S, Hanci G, Böhme M, et al. Effect of inoculum density on human-induced pluripotent stem cell expansion in 3D bioreactors. Cell Proliferation. 2019; 52: e12604.
10. Watson DC, Yung BC, Bergamaschi C, et al. Scalable, cGMP-compatible purification of extracellular vesicles carrying bioactive human heterodimeric IL-15/lactadherin complexes. J of Extracellular Vesicle. 2018; 7: 1442088.
11. Lambrechts T, Papantoniou I, Rice B, Schrooten J, Luyten FP, Aerts J-M. Large-scale progenitor cell expansion for multiple donors in a monitored hollow fibre bioreactor. Cytotherapy. 2016; 18: 1219–33.
12. Ala-Uotila S, Marjamäki A, Matikainen M-T, Jalkanen M. Use of a hollow fiber bioreactor for large-scale production of α2-adrenoceptors in mammalian cells. Journal of Biotechnology. 1994; 37: 179–84.
13. Yazaki PJ, Shively L, Clark C, et al. Mammalian expression and hollow fiber bioreactor production of recombinant anti-CEA diabody and minibody for clinical applications. Journal of Immunological Methods. 2001; 253: 195–208.
14. Jakl V, Ehmele M, Winkelmann M, et al. A novel approach for large-scale manufacturing of small extracellular vesicles from bone marrow-derived mesenchymal stromal cells using a hollow fiber bioreactor. Front Bioeng Biotechnol. 2023; 11: 1107055.
15. Garcia SG, Sanroque-Muñoz M, Clos-Sansalvador M, et al. Hollow fiber bioreactor allows sustained production of immortalized mesenchymal stromal cell-derived extracellular vesicles. Extracell Vesicles Circ Nucleic Acids. 2024; 5: 201–20.
16. Li Y, Wu Q, Wang Y, Li L, Bu H, Bao J. Senescence of mesenchymal stem cells (Review). International Journal of Molecular Medicine. 2017; 39: 775–82.
17. Neri S, Borzì R. Molecular Mechanisms Contributing to Mesenchymal Stromal Cell Aging. Biomolecules. 2020; 10: 340.
18. Ren G, Sørensen MB, Porsborg SR, Fink T, Zachar V, Peng Q. Comparative analysis of cryopreserved adipose stem cells expanded in hollow fiber bioreactor versus conventional tissue culture flasks. Sci Rep. 2024; 14: 31853.
19. Hou Y, Mi K, Sun L, et al. The Application of Hollow Fiber Cartridge in Biomedicine. Pharmaceutics. 2022; 14: 1485.
20. Bartosh TJ, Ylostalo JH. Efficacy of 3D Culture Priming is Maintained in Human Mesenchymal Stem Cells after Extensive Expansion of the Cells. Cells. 2019; 8: 1031.
21. Moya A, Paquet J, Deschepper M, et al. Human Mesenchymal Stem Cell Failure to Adapt to Glucose Shortage and Rapidly Use Intracellular Energy Reserves Through Glycolysis Explains Poor Cell Survival After Implantation. Stem Cells. 2018; 36: 363–76.
22. Chimenti I, Smith RR, Li T-S, et al. Relative Roles of Direct Regeneration Versus Paracrine Effects of Human Cardiosphere-Derived Cells Transplanted Into Infarcted Mice. Circulation Research. 2010; 106: 971–80.
23. Kizilay Mancini Ö, Lora M, Shum-Tim D, Nadeau S, Rodier F, Colmegna I. A Proinflammatory Secretome Mediates the Impaired Immunopotency of Human Mesenchymal Stromal Cells in Elderly Patients with Atherosclerosis. Stem Cells Translational Medicine. 2017; 6: 1132–40.
24. Naji A, Eitoku M, Favier B, Deschaseaux F, Rouas-Freiss N, Suganuma N. Biological functions of mesenchymal stem cells and clinical implications. Cell Mol Life Sci. 2019; 76: 3323–48.
25. Aggarwal S, Pittenger MF. Human mesenchymal stem cells modulate allogeneic immune cell responses. Blood. 2005; 105: 1815–22.
26. Ferrucci L, Fabbri E. Inflammageing: chronic inflammation in ageing, cardiovascular disease, and frailty. Nat Rev Cardiol. 2018; 15: 505–22.
27. Asumda FZ, Chase PB. Age-related changes in rat bone-marrow mesenchymal stem cell plasticity. BMC Cell Biol. 2011; 12: 44.
28. Wu J, Niu J, Li X, Wang X, Guo Z, Zhang F. TGF-β1 induces senescence of bone marrow mesenchymal stem cells via increase of mitochondrial ROS production. BMC Dev Biol. 2014; 14: 21.
29. Kim H-J, Ji B-R, Kim J-S, Lee H-N, Ha D-H, Kim C-W. Proteomic analysis of proteins associated with cellular senescence by calorie restriction in mesenchymal stem cells. In Vitro CellDevBiol-Animal. 2012; 48: 186–95.
30. Sun Y, Yu Y, Ma S, et al. Nanotube topography rejuvenates the senescence of mesenchymal stem cells by activating YAP signalling. J Mater Chem B. 2024; 12: 6917–26.
31. Páez J, Hernández R, Espinoza J, et al. Uncoupled inflammatory, proliferative, and cytoskeletal responses in senescent human gingival fibroblasts. J of Periodontal Research. 2020; 55: 432–40.
32. Dominici M, Le Blanc K, Mueller I, et al. Minimal criteria for defining multipotent mesenchymal stromal cells. The International Society for Cellular Therapy position statement. Cytotherapy. 2006; 8: 315–7.
33. Bianco P, Cao X, Frenette PS, et al. The meaning, the sense and the significance: translating the science of mesenchymal stem cells into medicine. Nat Med. 2013; 19: 35–42.
34. Théry C, Witwer KW, Aikawa E, et al. Minimal information for studies of extracellular vesicles 2018 (MISEV2018): a position statement of the International Society for Extracellular Vesicles and update of the MISEV2014 guidelines. J of Extracellular Vesicle. 2018; 7: 1535750.
35. Yeung C-YC, Dondelinger F, Schoof EM, et al. Circadian regulation of protein cargo in extracellular vesicles. Sci Adv. 2022; 8: eabc9061.
36. Bazié WW, Goyer B, Boucher J, et al. Diurnal Variation of Plasma Extracellular Vesicle Is Disrupted in People Living with HIV. Pathogens. 2021; 10: 518.
37. Kowal J, Arras G, Colombo M, et al. Proteomic comparison defines novel markers to characterize heterogeneous populations of extracellular vesicle subtypes. Proc Natl Acad Sci USA [Internet]. 2016 [cited 25 December 2025]; 113. Available at: https://pnas.org/doi/full/10.1073/pnas.1521230113
38. Théry C, Amigorena S, Raposo G, Clayton A. Isolation and Characterization of Exosomes from Cell Culture Supernatants and Biological Fluids. CP Cell Biology [Internet]. 2006 [cited 25 December 2025]; 30. Available at: https://currentprotocols.onlinelibrary.wiley.com/doi/10.1002/0471143030.cb0322s30
39. Muralidharan-Chari V, Clancy J, Plou C, et al. ARF6-Regulated Shedding of Tumor Cell-Derived Plasma Membrane Microvesicles. Current Biology. 2009; 19: 1875–85.
40. Jeppesen DK, Sanchez ZC, Kelley NM, et al. Blebbisomes are large, organelle-rich extracellular vesicles with cell-like properties. Nat Cell Biol. 2025; 27: 438–48.
41. Lim HJ, Yoon H, Kim H, et al. Extracellular Vesicle Proteomes Shed Light on the Evolutionary, Interactive, and Functional Divergence of Their Biogenesis Mechanisms. Front Cell Dev Biol. 2021; 9: 734950.
42. Gatto L, Lilley KS. MSnbase-an R/Bioconductor package for isobaric tagged mass spectrometry data visualization, processing and quantitation. Bioinformatics. 2012; 28: 288–9.
43. Aebersold R, Mann M. Mass-spectrometric exploration of proteome structure and function. Nature. 2016; 537: 347–55.
44. López-Otín C, Blasco MA, Partridge L, Serrano M, Kroemer G. The Hallmarks of Aging. Cell. 2013; 153: 1194–217.
45. Larsen M, Artym VV, Green JA, Yamada KM. The matrix reorganized: extracellular matrix remodeling and integrin signaling. Current Opinion in Cell Biology. 2006; 18: 463–71.
46. Herranz N, Gallage S, Mellone M, et al. mTOR regulates MAPKAPK2 translation to control the senescence-associated secretory phenotype. Nat Cell Biol. 2015; 17: 1205–17.
47. Salminen A, Kauppinen A, Kaarniranta K. Emerging role of NF-κB signaling in the induction of senescence-associated secretory phenotype (SASP). Cellular Signalling. 2012; 24: 835–45.
48. Freund A, Laberge R-M, Demaria M, Campisi J. Lamin B1 loss is a senescence-associated biomarker. Magin TM, Ed. MBoC. 2012; 23: 2066–75.
49. Stewart S, Darwood A, Masouros S, Higgins C, Ramasamy A. Mechanotransduction in osteogenesis. Bone & Joint Research. 2020; 9: 1–14.
50. Gaur M, Dobke M, Lunyak V. Mesenchymal Stem Cells from Adipose Tissue in Clinical Applications for Dermatological Indications and Skin Aging. IJMS. 2017; 18: 208.
51. Ahmad A, Braden A, Khan S, Xiao J, Khan MM. Crosstalk between the DNA damage response and cellular senescence drives aging and age-related diseases. Semin Immunopathol. 2024; 46: 10.
52. Coppé J-P, Patil CK, Rodier F, et al. Senescence-Associated Secretory Phenotypes Reveal Cell-Nonautonomous Functions of Oncogenic RAS and the p53 Tumor Suppressor. Downward J, Ed. PLoS Biol. 2008; 6: e301.
53. Mathieu M, Névo N, Jouve M, et al. Specificities of exosome versus small ectosome secretion revealed by live intracellular tracking of CD63 and CD9. Nat Commun. 2021; 12: 4389.
54. Basisty N, Kale A, Jeon OH, et al. A proteomic atlas of senescence-associated secretomes for aging biomarker development. Serrano M, Ed. PLoS Biol. 2020; 18: e3000599.
55. Tsukumo Y, Tomida A, Kitahara O, et al. Nucleobindin 1 Controls the Unfolded Protein Response by Inhibiting ATF6 Activation. Journal of Biological Chemistry. 2007; 282: 29264–72.
56. Fan W, Guo J, Gao B, et al. Flotillin-mediated endocytosis and ALIX–syntenin-1–mediated exocytosis protect the cell membrane from damage caused by necroptosis. Sci Signal. 2019; 12: eaaw3423.
57. Zhang D, Hua Z, Li Z. The role of glutamate and glutamine metabolism and related transporters in nerve cells. CNS Neurosci Ther. 2024; 30: e14617.

58. Liu F, Koval M, Ranganathan S, et al. Systems Proteomics View of the Endogenous Human Claudin Protein Family. J Proteome Res. 2016; 15: 339–59.
59. Wiley CD, Campisi J. The metabolic roots of senescence: mechanisms and opportunities for intervention. Nat Metab. 2021; 3: 1290–301.
60. Liang F, Lu X, Wu B, Yang Y, Qin W. Nucleolar Protein 56 Deficiency in Zebrafish Leads to Developmental Abnormalities and Anemia via p53 and JAK2-STAT3 Signaling. Biology. 2023; 12: 538.
61. Han H-M, Kim S-Y, Kim D-H. Mechanotransduction for therapeutic approaches: Cellular aging and rejuvenation. APL Bioengineering. 2025; 9: 021502.
62. Koh A, Mannerås-Holm L, Yunn N-O, et al. Microbial Imidazole Propionate Affects Responses to Metformin through p38γ-Dependent Inhibitory AMPK Phosphorylation. Cell Metabolism. 2020; 32: 643-653.e4.
63. Stępień EŁ, Durak-Kozica M, Kamińska A, et al. Circulating ectosomes: Determination of angiogenic microRNAs in type 2 diabetes. Theranostics. 2018; 8: 3874–90.
64. Zapała B, Kamińska A, Piwowar M, Paziewska A, Gala-Błądzińska A, Stępień EŁ. miRNA Signature of Urine Extracellular Vesicles Shows the Involvement of Inflammatory and Apoptotic Processes in Diabetic Chronic Kidney Disease. Pharm Res. 2023; 40: 817–32.
65. Kalluri R, LeBleu VS. The biology, function, and biomedical applications of exosomes. Science. 2020; 367: eaau6977.